Biomaterials Science

PAPER

View Article Online
View Journal | View Issue

Open Access Article. Published on 28 January 2022. Downloaded on 10/5/2024 8:24:09 PM.
This article is licensed under a Creative Commons Attribution 3.0 Unported Licence.

Check for updates

Cite this: *Biomater. Sci.*, 2022, **10**, 1554

Amyloid fibrils in superstructures – local ordering revealed by polarization analysis of two-photon excited autofluorescence†

Patryk Obstarczyk,[a] Maciej Lipok,[a] Andrzej Żak,[b] Paweł Cwynar[a] and Joanna Olesiak-Bańska*[a]

Received 19th November 2021,
Accepted 28th January 2022

DOI: 10.1039/d1bm01768c

rsc.li/biomaterials-science

Protein misfolding products – amyloids – tend to form distinct fibrillar structures of the characteristic fold for a given neurodegenerative disease or pathology. Moreover, amyloids (also in the intermediate or distorted state) can act as secondary nuclei for *de novo* fibrillation. Such secondary nucleation amplifies plaque development correlated with various diseases. Therefore, a versatile and non-destructive method of detection and differentiation between distinct fibrillar structures is of great importance. Amyloids exhibit unique optical properties, *i.e.* green-blue autofluorescence, which can also be induced by two-photon excitation. Herein, we use this label-free technique to resolve local fibrillar ordering in amyloid superstructures – spherulites. With polarization-dependent two-photon excited amyloid autofluorescence, we resolved fibrillar orientation in the spherulite corona and discussed the presence of amorphous aggregates, distorted fibrils or amyloid intermediate species within the spherulite core. Our polarization sensitive two-photon microscopy investigations are supported by TEM imaging and provide a promising tool for the detection and differentiation between well-developed amyloid fibrils and amorphous/distorted structures present at different stages of the formation of amyloid superstructures and plaques.

Introduction

Amyloids are defined as insoluble aggregates of misfolded proteins and peptides. Amyloidogenic proteins self-organize into fibrils distinguished by a repeatedly occurring motif of protein secondary structures – β-sheets – connected laterally by hydrogen bond networks.[1] The accumulation and deposition of amyloid fibrils in multiple organs are the hallmark of neurodegenerative diseases (ND), *e.g.* Parkinson's disease (PD), Alzheimer's disease (AD) and systemic disorders, including type II diabetes.[2] Diagnosis of the neurodegenerative diseases and investigation of their origin remain challenging due to the complexity of affected tissues, amyloid structural diversity and the requirement of non-destructive and complementary imaging techniques (*i.e.* light, atomic force and electron microscopy).[3,4] Recent developments in solid-state NMR spectroscopy and cryo-electron microscopy revealed *in vitro* and *ex vivo* amyloid fibril structures with near-atomic resolutions.[5] However, amyloid formation *in vivo*, toxicity and the influence on the pathological spreading rate of intermediate species (*e.g.* oligomers or protofibrils) still remain elusive due to the lack of methods able to fulfill the clinical diagnosis demands.[6–8] What is more, a growing amount of evidence suggests that amyloid oligomeric species and intermediate fibrillar structures are crucial in the pre-symptomatic phase of AD development and may enable rapid diagnosis if detected before plaque formation.[9]

Two-photon fluorescence microscopy (2PFM) provides high axial resolution because fluorophores outside of the focal plane are not excited, and it has lower scattering, reduced angular selection, lower phototoxicity of imaging and deeper optical penetration in comparison to one-photon excitation fluorescence microscopy techniques.[10,11] Therefore, 2PFM is indispensable for *in vivo* imaging and has been already implemented in an AD mouse model, where the significance of near-infrared probes (NIR) for deep-tissue imaging was demonstrated.[12] Moreover, polarization sensitive two-photon fluorescence microscopy (ps-2PFM) was already proven to be successful in the determination of the orientational ordering of thioflavin-T (ThT) stained amyloid fibrils by our group,[13]

---

[a] *Advanced Materials Engineering and Modelling Group, Faculty of Chemistry, Wrocław University of Science and Technology, Wybrzeże Wyspaińskiego 27, 50-370 Wrocław, Poland. E-mail: joanna.olesiak@pwr.edu.pl*
[b] *Electron Microscopy Laboratory, Faculty of Mechanical Engineering, Wrocław University of Science and Technology, Wybrzeże Wyspaińskiego 27, 50-370 Wrocław, Poland*

† Electronic supplementary information (ESI) available: Polarized light optical microscopy images of unlabeled and ThT-labelled spherulites with crossed polarizers and the panoramic TEM image of the entire spherulite structure (PDF). See DOI: 10.1039/d1bm01768c

This journal is © The Royal Society of Chemistry 2022

Open Access Article. Published on 28 January 2022. Downloaded on 10/5/2024 8:24:09 PM. This article is licensed under a Creative Commons Attribution 3.0 Unported Licence.

being in good agreement with the one-photon polarization analysis of the Brasselet group.[4] However, well known amyloid staining dyes ThT and Congo red (CR) as well as many new fluorophores designed to stain amyloids display increased fluorescence due to hindrance in the free rotation of the dyes upon binding or molecular-docking to β-sheet structures.[14] Thus, the binding mechanism hinders the sensitivity of ThT and CR for fibrillar intermediates. Therefore, the development of new probes for the detection of various forms of amyloids other than fully developed fibrils is of great importance.[15]

Amyloids, even in protein systems devoid of aromatic amino acids, possess unique optical properties, *i.e.* blue-green autofluorescence (AF), with a mechanism which is still not fully understood.[16,17] This autofluorescence in amyloids can also be induced by two-photon excitation, which provides new opportunities for *in vivo* bio-imaging.[18,19] Imaging based on the intrinsic fluorescence of amyloids is beneficial, since it is highly dependent on the aggregation state and may contain structural information, disturbed or not detected by fluorescent probes.[20] Our group has already contributed to the field and reported two-photon excited polarized amyloid autofluorescence (2PAF) in bovine insulin fibrils.[13] Herein, we further explore 2PAF as a versatile tool for resolving three-dimensional fibrillar organization and most importantly – ordering in amyloid spherulites, which are spherical structures (from 5 to 150 μm in diameter) built from β-sheet rich amyloidogenic protein aggregates, whose origin and biological role are still poorly described.[18,21] Amyloid spherulites were found in the *post-mortem* brains of AD, PD and Creutzfeldt–Jakob disease patients.[21] Moreover, due to the tissue preparative methodology (thin sectioning) spherulites may be overlooked in *ex vivo* samples.[22] They present a unique structure, where the non-birefringent core is radially decorated by highly ordered fibrils.[23,24] Thus, they contain amyloid fibrils at various stages of organization. Herein, we show that ps-2PFM can provide information about fibril orientation and ordering in individual spherulites, which are complex and densely packed and have a wet environment, which is important in the translation of the technique to *in vivo* conditions. We present the aberrations of the conical distribution of the emission dipole of 2PAF in amyloid spherulites as a novel means to detect amyloid fibrils and amyloid intermediate state orientation and molecular ordering.

Results and discussion

Unlabelled and ThT-stained amyloid spherulites from bovine insulin powder were prepared as described in the Experimental section. Aliquots of solutions containing spherulites were investigated by polarization optical microscopy and well-separated spherical particles of overall diameter ranging from 10 to 90 μm were observed. Observations conducted with crossed polarizers revealed characteristic Maltese-cross extinction patterns, as presented in the ESI (Fig. S1†). The core of each spherulite appeared to be non-birefringent, which is in agreement with previous reports.[23] Polarization-sensitive two-photon fluorescence microscopy (ps-2PFM) was used for spherulite imaging (details are available in the Experimental section and ref. 13). Solutions containing spherulites were illuminated with horizontally and vertically polarized incident light (with reference to the *XY* microscope sample plane) and two-photon excited fluorescence (2PF) was split in horizontally (I_X) and vertically (I_Y) polarized components, collected and analyzed. Due to the photo-selection, the highest emission intensity is expected to be observed when the transition dipole moment of the fluorophore is aligned parallel to the polarization of the incident light, which is represented by 2PAF intensity distribution on the *XY* microscope sample plane (Fig. 1a). Several spots from distinct spherulites, as denoted on grey scale maps (Fig. 1a), were chosen to perform full polarization analysis of two-photon excited autofluorescence (denoted as AF) and thioflavin-T fluorescence (denoted as ThT) to resolve the sub-μm scale of amyloid fibril ordering. Examples of collected data and fitting results are presented in the form of I_{2PF} polar graphs collected in the *X* and *Y* directions (red and blue points, respectively) (Fig. 1b). A similar procedure can be applied for any position in the spherulite. The rotation of the fibrils in the *XY* microscopic sample plane is described by the Φ angle. The half angle Ψ corresponds to the conical distribution of the emission dipole of the fluorescent species. For amyloid autofluorescence it was determined to be equal to 29° around the long axis of the insulin fibrils.[13] Aberrations of Ψ arising from molecular rotations, therefore contributing to the molecular ordering, are described by $\Delta\Psi$. Comprehensive description of the open cone model used for data analysis and fitting was given previously,[13] and is schematically represented in Fig. 1c.

Cones constructed from black (Φ) and green arrows ($\Psi + \Delta\Psi$, where Ψ is set to 29° and is constant and $\Delta\Psi$ is ranging from 15° to 31°) are plotted in Fig. 2a and point the position of amyloid fibrils in the *XY* microscopic plane which corresponds to spots starting from the structure core and localized along the spherulite radius (as denoted by a white arrow on the grey scale I_{2PF} map). The presented results confirm the radial orientation of amyloid fibrils in the highly organized areas of spherulites (cones no. 5–9), being consistent with the observations of Krebs *et al.*[23] However, the differences in the direction (Φ) and size of plotted cones ($\Psi + \Delta\Psi$) are visible between points no. 1–4, 5–7 and 8–9. Thus, three regions of distinct organization were observed on the spherulite radius (Fig. 1b). The first (cones no. 1–3) is located within the spherulite core, and two (cones no. 5–7, and 8–9) in the spherulite inner and outer corona, respectively. The possibility to measure highly polarized 2PAF within the spherulite core, where fibrils are not expected to be present, raises a question about the origin of autofluorescence and will be addressed in further paragraphs.

In order to quantitatively determine the degree of ordering in various regions of a spherulite, we extracted $\Delta\Psi$ values from the polarization analysis in selected points across un-labeled spherulite radii and compared them with the data from the

Open Access Article. Published on 28 January 2022. Downloaded on 10/5/2024 8:24:09 PM.
This article is licensed under a Creative Commons Attribution 3.0 Unported Licence.

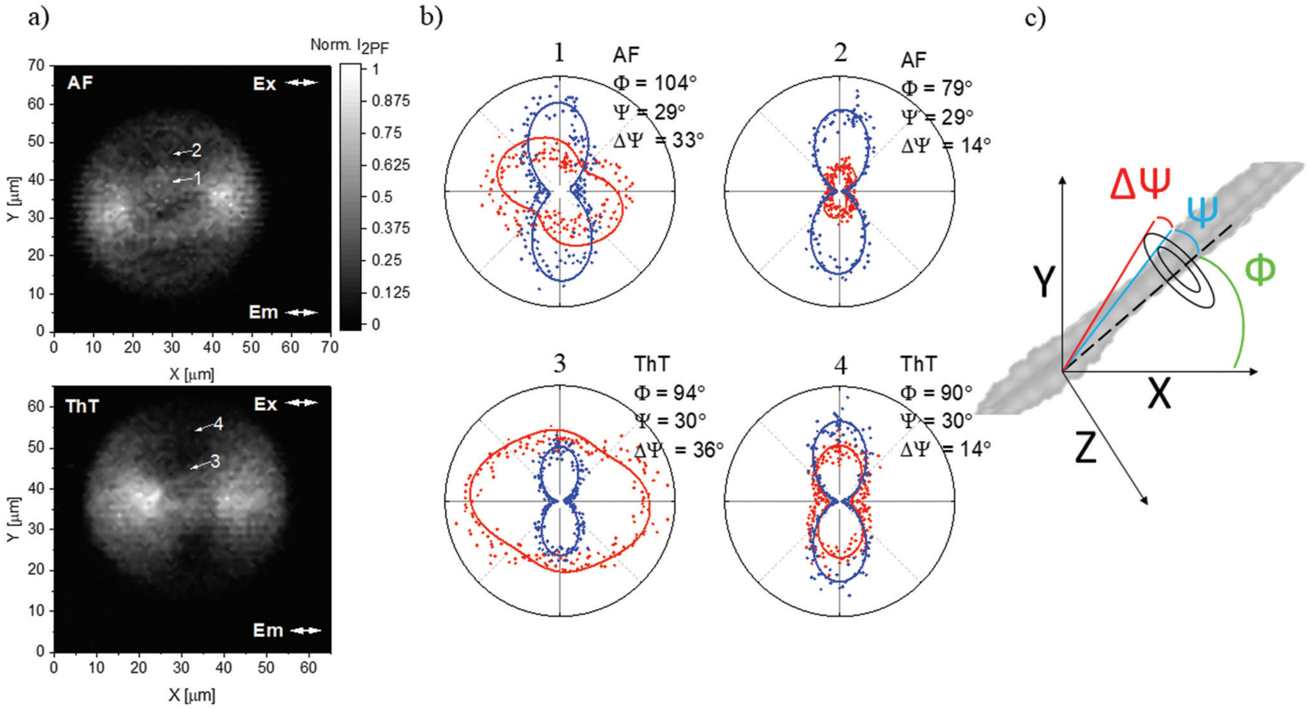

Fig. 1 (a) Grey scale map presenting two-photon excited amyloid autofluorescence (AF) and ThT fluorescence (ThT) intensity distribution. Polarization of the excitation beam (Ex) and emission (Em) is denoted with double-headed arrows, and the excitation wavelength was set to 810 nm. (b) Exemplary polar graphs from the spots denoted on grey scale maps. Experimental datasets are presented as dots (I_X and I_Y components are red and blue, respectively) and solid lines present the fitting of the angular dependence of the X and Y components of two-photon excited emission. (c) Schematic representation of Ψ, $\Delta\Psi$ and Φ angles in the XY microscopic sample plane.

polarization analysis of the 2PF of ThT-labeled spherulites (Fig. 2b). As previously reported, ThT binds perpendicularly to the β-strands of amyloid fibrillar structures (*i.e.* parallel to the amyloid fibril long axis), and thus it reproduces fibril orientation.[25,26]

Based on 2PF intensity profiles and the sigmoidal shape of $\Delta\Psi$ value plots (black curves, Fig. 2b), three regions of distinct fibrillar orientation can be observed, corresponding to the core- (yellow shading – R_1), inner- (red shading – R_2) and outer-corona (blue shading – R_3) for ThT-labeled and label-free spherulites. $\Delta\Psi$ values decrease radially from the core to the periphery, *i.e.* the outer-corona region, as presented in Fig. 2b. The degree of fibril organization is inversely proportional to $\Delta\Psi$, and thus we can indicate the unorganized core and highly organized periphery of a spherulite. High disorder in the R_1 region is clearly visible, with the $\Psi + \Delta\Psi$ average value equal to 70° and 64.5° for 2PAF and ThT 2PF, respectively. Ordering increases between the R_2 and R_3 regions, where $\Psi + \Delta\Psi$ values are equal to 51.5° and 53° for 2PAF and ThT 2PF, respectively. Moreover, the $\Delta\Psi$ values of 2PAF seem to change more drastically in the R_2 region, in comparison to $\Delta\Psi$ assigned to the 2PF of ThT. The sigmoidal shape of the $\Delta\Psi$ (R) plots in both cases reveals the complex structure of amyloid spherulites where a transition from the unorganized core (R_1) to the highly organized outer corona (R_3) is preceded by the intermediate state with fibrils at various states of organization (R_2).

Intensity profiles across the unlabeled and ThT-stained spherulites of similar sizes are presented in Fig. 3. The ThT 2PF intensity clearly decreases by ~80% near to the amorphous core, where the 2PAF intensity decreases only by ~60%. Amyloid spherulites may grow from the nucleus, which is in the form of amorphous aggregates, or starting from the collapse and disorganization of the fibrils.[23] As all fibrils present autofluorescence, disorganized fibrils in the spherulite core are probably well detected by 2PAF in our experiments. However, disorganization and collapse of the fibrils may be responsible for the significant decrease of ThT fluorescence intensity in the core. Due to the binding modes of ThT, the intermediate states of fibrils cannot be properly stained,[27] which is further confirmed by extensive research on the improvement of imaging agents to detect amyloid accumulation.[9] High 2PAF allowing the estimation of the molecular ordering degree in the spherulite core might also be assigned to amorphous and distorted structures or even oligomeric species present in the initial stages of the formation of amyloid fibrils and superstructures.[28]

In order to support our findings, we decided to compare the fibrillar structure of spherulites probed *via* ps-2PFM and transmission electron microscopy (TEM). The amyloid spherulite solution for TEM imaging was fixed, dehydrated, embedded in a resin and cut in ultra-thin (80 nm) sections. Detailed TEM sample preparation description is available in

Open Access Article. Published on 28 January 2022. Downloaded on 10/5/2024 8:24:09 PM.
This article is licensed under a Creative Commons Attribution 3.0 Unported Licence.

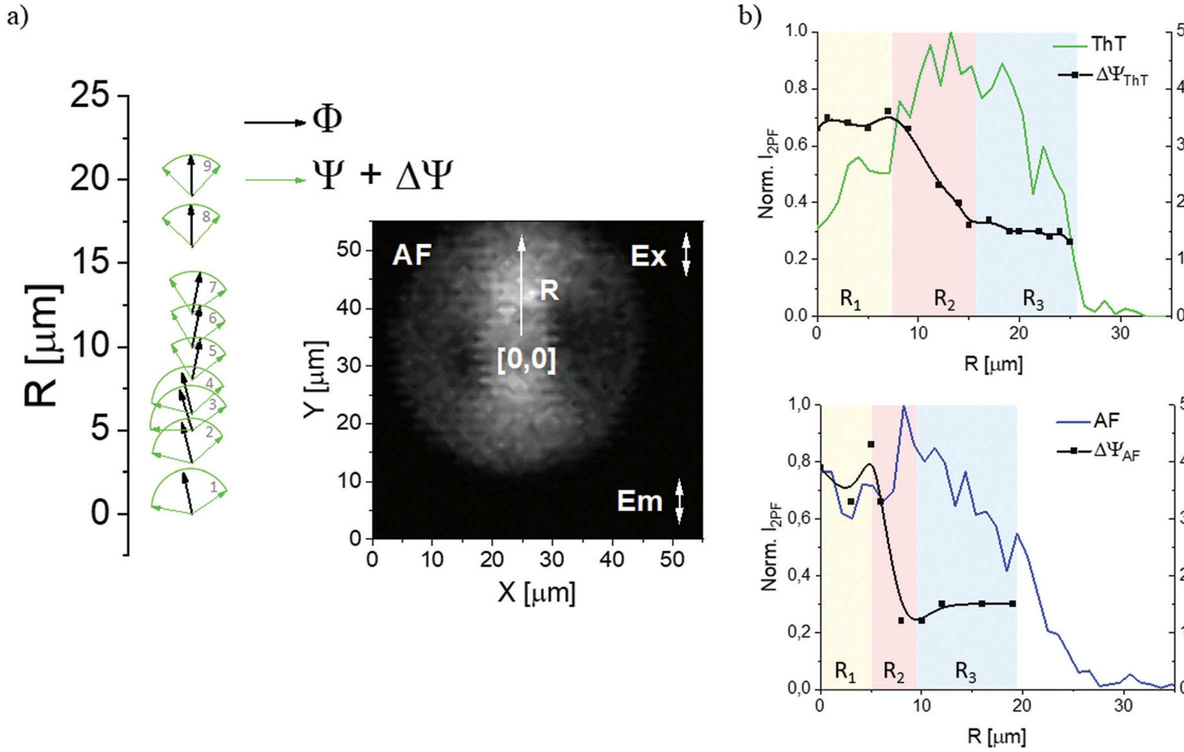

Fig. 2 (a) Fibril direction on the spherulite radius, marked as a single-headed white arrow – *R* – described by the *Φ* angle. The radius starts from the spherulite core and ends on the structure periphery. (b) Aberrations of the conical distribution of the direction of the emission dipole of the fluorophore – Δ*Ψ* – correlated with the spherulite radius of the label-free (blue line) and ThT-labeled (green line) samples. The *Ψ* values are 30° and 29° for ThT and AF, respectively.

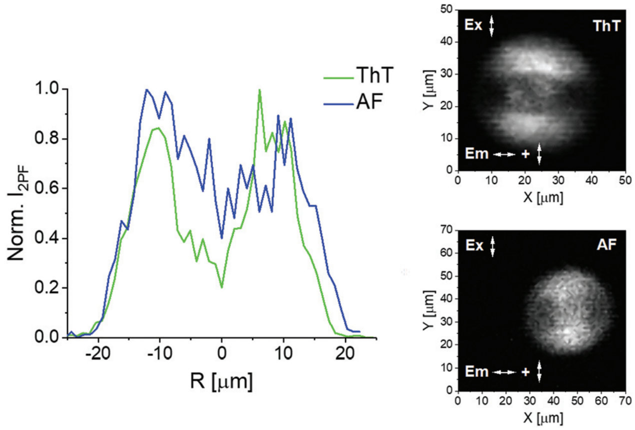

Fig. 3 Two-photon excited fluorescence intensity profiles of the label-free (blue line) and ThT-labeled (green line) pairs of spherulites. The horizontal axis – *R* – corresponds to the spherulite radius starting from the structure center to the periphery. Insets present 2PF intensity raster scans as a sum of horizontally and vertically polarized emission components.

the Experimental section. At low magnifications, the spherulite outer border did not stand out sharply from the background. However, it can be determined whether the observed cross-section runs through the center of the spherulite or only through its edge. In the case of an eccentric cross-section, the fibrous structure and amorphous structures of the core are not clearly visible. The correct structure of the diameter cross-section through the spherulite can be observed in Fig. 4a. Larger magnifications allowed for a precise description of the ultrastructure (Fig. 4b), where four regions can be distinguished. The characteristic structural regions are marked as I–IV in Fig. 4b. The core (I) consists of tightly entangled and disorganized fibrils which are arranged in micrometric-wide, parallel strands. Moreover, highly contrasted areas consisting of non-fibrillar shapes are also clearly visible (Fig. 4f), which may be identified as amorphous aggregates. The tightest packing on the scale of the entire TEM imaged spherulite has a radius of around 5 μm. As the fibers move away from the core, they form a radial, but partially tangled and densely packed structure (II), which gives way to a loosely packed and more organized fibrillar structure (III). The rising degree of organization may be explained by secondary nucleation on or between the already grown fibrils, which raises questions about spherulite formation mechanisms. In the spherulite outer region fibrils bend by 45° (IV). The parallel arrangement of the fibrils is present together with fibrils oriented in multiple directions. Region no. IV of the spherulite is about 1.5 μm thick, and its outer surface is about 300 nm thick. It can be concluded that the core is tightly packed (Fig. 4f) and the density of the radially organized structures (Fig. 1e) decreases with the dis-

Open Access Article. Published on 28 January 2022. Downloaded on 10/5/2024 8:24:09 PM.
This article is licensed under a Creative Commons Attribution 3.0 Unported Licence.

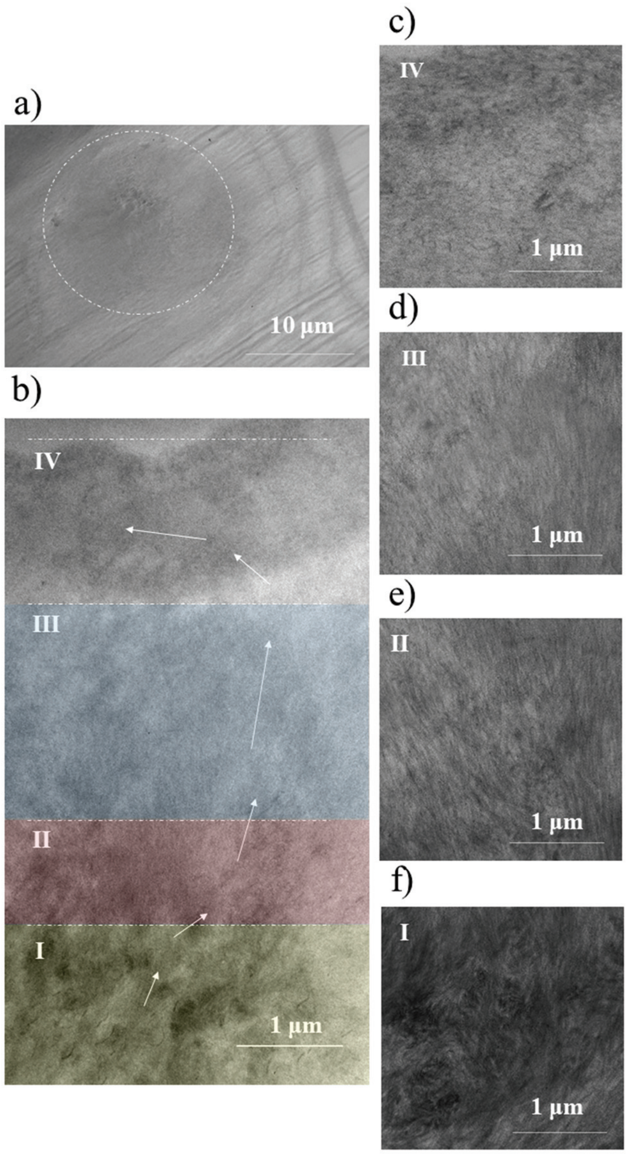

Fig. 4 (a) TEM macroscopic view of spherulites in the central cross-section. (b) Cross-section fragment with an example of a fibril course (arrows) and characteristic elements of the structure: I – a densely packed core consisting of a micrometric width of bundles of tangled fibrils and intermediate states, II – a tightly packed area of tangled fibrils, III – a loosely packed area of fibrils, and IV – shell forming fibrils. Magnified view of (c) IV, (d) III, (e) II, and (f) I regions. The panoramic TEM image of the entire structure is available in the ESI (Fig. S2†).

tance from the core. The density increases again only after the fibrils fold parallel to the outer surface (Fig. 4d) and increases even more in the outer shell, separating the interior from the environment (Fig. 4c). One should note that TEM sample preparation, including dehydration, influences the observed structures despite fixation. Removal of water may contribute to the formation of a shell. An intense fibril twist should be easily detected by varying the polarization of incident light. However, fibrillar bending near the spherulite edge was not observed in the samples under investigation with ps-2PFM, which supports the hypothesis of structural changes induced only in TEM imaging by fixation and dehydration.

The spherulite core observed by TEM (region I) is densely packed and consists of a micrometric width of bundles of tangled fibrils and intermediate states. Fibrils from the core are disorganized and probably distorted structurally, which explains a high decrease of ThT 2PF in this region. However, the distortion of the fibrils and the presence of intermediate states still allow autofluorescence, and thus high 2PAF is detected for the corresponding region under ps-2PFM (*i.e.* R_1). Previous results of optical microscopy correlated with the Raman scattering spectroscopy of spherulites published by the A. M. Donald group[29] show that the β-sheet content in the spherulites varies from 75% near the edge to 60% in the core. The random coil content is ranging from 15% to 25% near the edge and in the core, respectively, and the remaining percentage is assigned to α-helix structures. Our experiments are in good agreement with these observations since a significant β-sheet percentage content in the spherulite core may be assigned to the fibrils detected by TEM imaging and the high values of $\Delta\Psi$ observed for this region may originate from the amorphous structures or intermediate fibrillar structures, and therefore distinguish these states from the fully developed fibrils.

Observations of the spherulite inner and outer corona under TEM are in agreement with ps-2PFM, where two regions of slightly different fibril orientation (Φ angle) were detected (R_2 and R_3, which correspond to region no. II, and III from TEM imaging, respectively). Region no. III, of the lowest density (R_3 from ps-2PFM), is characterized by the highest degree of organization where clearly visible fibrils are radially oriented. Region II, of high density, corresponds to the inner-corona region (R_2 from ps-2PFM) and is more disordered, therefore fibril presence and orientation are harder to determine from the TEM image, which is in good agreement with the higher $\Delta\Psi$ values (in comparison to III, R_3) from ps-2PFM.

The structural diversity of amyloid fibrils is nowadays linked to different pathologies, as the amount of evidence is rapidly growing.[30] Recognition of the intermediate states of protein aggregates, at various stages of organization, is limited due to the insufficiency of current methodologies, usually based on the staining procedure further dependent on the dye to fibril binding mechanisms. Numerous intermediate states and amorphous structures can induce distortion detected by polarization analysis, being simultaneously non-reflected by the interaction with staining agents, which is advantageous if structure dependent two-photon excited autofluorescence is used. Based on sedimentation experiments and the constant density of the spherulites with respect to their radius, Rogers *et al.*[31] suggested that the space in the spherulite corona must be filled by branched structures, otherwise a constant density over the entire structure cannot be maintained. However, in our results amyloid branching is not observed *via* TEM or ps-2PFM imaging. Both imaging techniques revealed radial orien-

Open Access Article. Published on 28 January 2022. Downloaded on 10/5/2024 8:24:09 PM.
This article is licensed under a Creative Commons Attribution 3.0 Unported Licence.

tation of fibrils within superstructures, which corresponds well to the results obtained by T. Hiramatsu *et al.* based on the coincided direction of the dark sections and that of the analyzer axis under a polarized light microscope.[32]

To further discuss the observed variations of $\Delta\Psi$ within the radius of a single aggregate, we suggest that spherulites should be considered as dense and heterogenous structures filled with amyloids at various states of aggregation, concentration and organization. Differences between the core and superstructure corona revealed by our ps-2PAF analysis correspond well to the combined FLIM and micro-FTIR studies by G. De Luca *et al.*, where H-bond coupling differed and changed in dependence of the position within a single spherulite indicating its intrinsic heterogeneity.[33] Moreover, *in situ* Raman imaging of amyloid aggregates by M. Ishigaki *et al.* confirmed the presence of various polymorphs within insulin spherulite-like structures, based on the analysis of the relative proportion of β-sheet structures, the intensity ratio of the tyrosine doublet and the signal intensity arising from the disulfide bonds.[34] A drastic drop of the ThT fluorescence intensity near the core suggests that even though mature fibrils may be present there, the dye is not capable of properly staining them. We hypothesize that the aforementioned limitation may arise from the lack of accessibility of ThT molecules to fibrils formed *de novo* inside the core, or due to distortion of the binding sites of polymorphs formed in the initial state of superstructure growth. Therefore, non-negligible heterogeneity of the spherulites detected within sub-micron spatial resolution may arise from multiple interconnected aggregation pathways. The coherent ps-2PFM and TEM images of the bovine insulin spherulite structure suggest a secondary nucleation event in the amyloid superstructure formation process. Differences between the inner- and outer-corona regions distinguished by $\Delta\Psi$, as well as the packing density visible under TEM imaging, may arise from colinear fibril growth between the initially formed ones or the *de novo* formation from fibril derived oligomers. What is more, TEM observations confirmed the presence of unorganized and probably highly distorted fibrillar structures in the spherulite core, which correspond to high 2PAF and the decrease of ThT 2PF.

Conclusions

We show that two-photon excited autofluorescence polarization analysis (ps-2PAF) of amyloids may be used to detect fibril orientation in a sub-micron size regime and the results are coherent with previous studies on amyloid spherulite organization. Our results indicate that a single spherulite is highly heterogenous and its structural components are gradually changing across its radius, where the highest organization is observed near the edges. Moreover, ps-2PAF gives information about the aberration of the conical distribution of the emission dipole of the autofluorescence, which may serve as an indicator of the amyloid fibril distortion and structural heterogeneity. It is of great importance for the detection of structures present at the initial stages of the formation of amyloid superstructures and plaques. Comparison of ThT-stained and unlabeled spherulites showed that the cores of spherulites present low ThT fluorescence, but still significant autofluorescence. Thus, sole ThT molecules docked in fully-developed fibrils are contributing to the collected 2PF signal, and thus, ThT application in the detection of distorted or amorphous amyloid intermediate fibrillar states is limited. Analysis of conical distribution aberration reveals structural information about protein aggregates which are masked or not available *via* the currently applied methodologies, which can be used for investigation on numerous anisotropic biological systems. Moreover, our stain-free method is not limited by dye affinity or accessibility to the binding sites, and thus can detect transient species, which is of great importance in the field and may contribute to the understanding of the diverse pathways of protein and peptide aggregation. TEM imaging performed on spherulites was consistent with polarization-sensitive two-photon microscopy investigations. TEM images confirmed the presence of fibril intermediates in the spherulite core, well-detected by 2PAF. Therefore, our technique is promising for the detection and differentiation of amyloid fibrils disordered and intermediate states from fully-developed ones, as well as detail organization of the latter fibrils. Our work broadens the knowledge about amyloid autofluorescence, aggregation and organization imaging.

Experimental section

Chemicals

Insulin from bovine pancreas (≥25 units per mg (HPLC), I5500), DPX mountant for histology (slide mounting medium), sodium chloride (≥99%), hydrochloric acid (≥37%, APHA: ≤10), glutaraldehyde, osmium tetroxide, uranyl acetate, ethanol, acetone (Sigma-Aldrich) and Epon 812 (AgarScientific) were used without further purification. All organic solvents were HPLC grade, ≥99.9%. High-purity water (Milli-Q, resistivity <0.06 μS cm^{-1}) was used throughout all the experiments.

ps-2PFM sample preparation

Solutions were prepared by dissolving 10 mg of bovine insulin powder in 1 mL of water mixture with pH adjusted to 1.5 (with hydrochloric acid) in 1.5 mL Eppendorf Safe-Lock Tubes (polypropylene). The salt (sodium chloride) concentration was set to 10 mM. Thioflavin T-labeled spherulites were prepared with an additional portion of 0.05 mg of ThT dye. The solutions were incubated at 70 °C for 24 h without stirring (in an Eppendorf Thermomixer C). Spherulite containing solutions (~100 μL) were pipetted in microscope slides with wells (Super White Glass, 76 × 26 × 1 mm, CHEMLAND) and then covered with a coverslip (Super White Glass, EQUIMED). The as-prepared samples were sealed thoroughly with DPX mountant near glass edges and left for 12–24 h at 5 °C for the mountant to harden.

Open Access Article. Published on 28 January 2022. Downloaded on 10/5/2024 8:24:09 PM.
This article is licensed under a Creative Commons Attribution 3.0 Unported Licence.

ps-2PFM setup

ps-2PFM was performed with a multiphoton microscope and a polarization-sensitive detection path described in our previous work.[13] The excitation light source was a fs mode-locked Ti: Sapphire laser (~100 fs, 80 MHz, Chameleon, Coherent Inc.). The polarization of excitation light was controlled with a half-wave plate mounted on a rotation stage. The samples were mounted on an XYZ piezoelectric scanning stage (Piezojena, TRITOR 102) and scanned. The polarized laser beam was reflected using a dichroic mirror and focused on the sample. A high-numerical aperture objective was used (Nikon Plan Apo Oil Immersion 100×/1.4 NA). The emitted signal (epifluorescence mode) was collected by the same objective and split by a polarizing beam-splitter into two orthogonally polarized beams (I_X and I_X) to be detected by two photon-counting avalanche photodiodes (IDQ id100). The signals from the samples were obtained with the excitation wavelength set to 810 nm, and the power of the incident laser beam was set within 100–900 μW to 10–50 μW for auto-fluorescence measurements and thioflavin-T labeled spherulites, respectively.

Data fitting model

A comprehensive applied theory description and calculation protocol (based on a Phyton custom-made script) is available in our previous work published in the open-access format.[13] Data fitting was performed with fixed values of Ψ being set to 30° and 29° for ThT and autofluorescence, respectively, as determined in ref. 13.

TEM imaging and sample preparation

All solutions were prepared in 1.5 mL Eppendorf Safe-Lock tubes (polypropylene). For TEM imaging spherulites were fixed in 2% glutaraldehyde (for 24 h), and then post-fixed with 1% osmium tetroxide for 30 min. The sample was then dehydrated *via* an acetone series up to 100% acetone, infiltrated with 50% and 100% Epon 812 resin and polymerized at 60 °C overnight. The hardened resin block was trimmed and 80 nm ultrathin sections were cut. The sections were collected on clean copper grids (AgarScientific, AGG2200C) and stained with 0.5% uranyl acetate. Small spherulites with the diameter corresponding to the maximal size of copper grid windows were found and identified with a light microscope and then imaged with a TEM (Hitachi H-800, a 200 kV thermal emission microscope, equipped with a tungsten filament and an EMSIS Quemesa CCD camera).

Abbreviations

PD	Parkinson's disease
AD	Alzheimer's disease
ThT	Thioflavin-T
AF	Autofluorescence
ps-2PFM	Polarization-sensitive two-photon fluorescence microscopy
TEM	Transmission electron microscopy
2PF	Two-photon fluorescence
ND	Neurodegenerative diseases
2PFM	Two-photon fluorescence microscopy
CR	Congo red
2PAF	Two-photon autofluorescence

Author contributions

P. O. prepared spherulite solutions and sealed microscope samples, measured and analysed the data from ps-2PFM and prepared the original draft of the manuscript. M. L. performed the fitting of the angular dependence of the X and Y components of two-photon excited emission. A. Z. performed the imaging of TEM samples. P. C. helped with the initial protocol development for the spherulite incubation. J. O. B. acquired the funding, and analysed the data as well as formulated the research goals and supervised the research. All authors took part in writing the manuscript, review and editing of its text.

Conflicts of interest

There are no conflicts to declare.

Acknowledgements

This work was supported by the NONA project (First TEAM/2017-3/27) carried out within the First Team program of the Foundation for Polish Science and co-financed by the European Union under the European Regional Development Fund. Andrzej Żak would like to thank MSc Sylwia Nowak and the Laboratory of Microscopic Techniques, Faculty of Biological Sciences, University of Wroclaw for help with the TEM sample preparation.

Notes and references

1 P. C. Ke, R. Zhou, L. C. Serpell, R. Riek, T. P. J. Knowles, H. A. Lashuel, E. Gazit, I. W. Hamley, T. P. Davis, M. Fändrich, D. E. Otzen, M. R. Chapman, C. M. Dobson, D. S. Eisenberg and R. Mezzenga, *Chem. Soc. Rev.*, 2020, **49**, 5473–5509.

2 M. G. Iadanza, M. P. Jackson, E. W. Hewitt, N. A. Ranson and S. E. Radford, *Nat. Rev. Mol. Cell Biol.*, 2018, **19**, 755–773.

3 U. Cendrowska, P. J. Silva, N. Ait-Bouziad, M. Müller, Z. P. Guven, S. Vieweg, A. Chiki, L. Radamaker, S. T. Kumar, M. Fändrich, F. Tavanti, M. C. Menziani, A. Alexander-Katz, F. Stellacci and H. A. Lashuel, *Proc. Natl. Acad. Sci. U. S. A.*, 2020, **117**, 6866–6874.

4 J. Duboisset, P. Ferrand, W. He, X. Wang, H. Rigneault and S. Brasselet, *J. Phys. Chem. B*, 2013, **117**, 784–788.

5 M. Kollmer, W. Close, L. Funk, J. Rasmussen, A. Bsoul, A. Schierhorn, M. Schmidt, C. J. Sigurdson, M. Jucker and M. Fändrich, *Nat. Commun.*, 2019, **10**, 4760.

This journal is © The Royal Society of Chemistry 2022

Open Access Article. Published on 28 January 2022. Downloaded on 10/5/2024 8:24:09 PM.
This article is licensed under a Creative Commons Attribution 3.0 Unported Licence.

6 R. Kayed and C. A. Lasagna-Reeves, *J. Alzheimer's Dis.*, 2013, **33**(Suppl 1), S67–S78.

7 M. Diociaiuti, R. Bonanni, I. Cariati, C. Frank and G. D'Arcangelo, *Int. J. Mol. Sci.*, 2021, **22**(12), 6435.

8 X. Zhang, Y. Tian, C. Zhang, X. Tian, A. W. Ross, R. D. Moir, H. Sun, R. E. Tanzi, A. Moore and C. Ran, *Proc. Natl. Acad. Sci. U. S. A.*, 2015, **112**, 9734–9739.

9 H. Liu, J. Yang, L. Wang, Y. Xu, S. Zhang, J. Lv, C. Ran and Y. Li, *Future Med. Chem.*, 2017, **9**, 179–198.

10 K. Svoboda and R. Yasuda, *Neuron*, 2006, **50**, 823–839.

11 W. R. Zipfel, R. M. Williams and W. W. Webb, *Nat. Biotechnol.*, 2003, **21**, 1369–1377.

12 C. Chen, Z. Liang, B. Zhou, X. Li, C. Lui, N. Y. Ip and J. Y. Qu, *ACS Chem. Neurosci.*, 2018, **9**, 3128–3136.

13 P. Obstarczyk, M. Lipok, M. Grelich-Mucha, M. Samoć and J. Olesiak-Bańska, *J. Phys. Chem. Lett.*, 2021, **12**, 1432–1437.

14 M. Biancalana and S. Koide, *Biochim. Biophys. Acta*, 2010, **1804**, 1405–1412.

15 A. Aliyan, N. P. Cook and A. A. Martí, *Chem. Rev.*, 2019, **119**, 11819–11856.

16 L. Grisanti, M. Sapunar, A. Hassanali and N. Došlić, *J. Am. Chem. Soc.*, 2020, **142**, 18042–18049.

17 D. Pinotsi, L. Grisanti, P. Mahou, R. Gebauer, C. F. Kaminski, A. Hassanali and G. S. Kaminski Schierle, *J. Am. Chem. Soc.*, 2016, **138**, 3046–3057.

18 P. K. Johansson and P. Koelsch, *Biomed. Opt. Express*, 2017, **8**, 743–756.

19 P. Hanczyc, M. Samoc and B. Norden, *Nat. Photonics*, 2013, **7**, 969–972.

20 M. Grelich-Mucha, A. M. Garcia, V. Torbeev, K. Ożga, Ł. Berlicki and J. Olesiak-Bańska, *J. Phys. Chem. B*, 2021, **125**, 5502–5510.

21 C. Exley, E. House, J. F. Collingwood, M. R. Davidson, D. Cannon and A. M. Donald, *J. Alzheimer's Dis.*, 2010, **20**, 1159–1165.

22 E. House, K. Jones and C. Exley, *J. Alzheimer's Dis.*, 2011, **25**, 43–46.

23 M. R. H. Krebs, C. E. MacPhee, A. F. Miller, I. E. Dunlop, C. M. Dobson and A. M. Donald, *Proc. Natl. Acad. Sci. U. S. A.*, 2004, **101**, 14420–14424.

24 M. I. Smith, V. Foderà, J. S. Sharp, C. J. Roberts and A. M. Donald, *Colloids Surf., B*, 2012, **89**, 216–222.

25 B. Frieg, L. Gremer, H. Heise, D. Willbold and H. Gohlke, *Chem. Commun.*, 2020, **56**, 7589–7592.

26 M. Biancalana and S. Koide, *Biochim. Biophys. Acta, Proteins Proteomics*, 2010, **1804**, 1405–1412.

27 M. I. Sulatsky, A. I. Sulatskaya, O. I. Povarova, I. A. Antifeeva, I. M. Kuznetsova and K. K. Turoverov, *Prion*, 2020, **14**, 67–75.

28 A. Bhattacharya, S. Bhowmik, A. K. Singh, P. Kodgire, A. K. Das and T. K. Mukherjee, *Langmuir*, 2017, **33**, 10606–10615.

29 D. Cannon, S. J. Eichhorn and A. M. Donald, *ACS Omega*, 2016, **1**, 915–922.

30 D. Li and C. Liu, *Nat. Chem. Biol.*, 2021, **17**, 237–245.

31 S. S. Rogers, M. R. H. Krebs, E. H. C. Bromley, E. van der Linden and A. M. Donald, *Biophys. J.*, 2006, **90**, 1043–1054.

32 T. Hiramatsu, N. Yamamoto, S. Ha, Y. Masuda, M. Yasuda, M. Ishigaki, K. Yuzu, Y. Ozaki and E. Chatani, *Sci. Rep.*, 2020, **10**, 16741.

33 G. De Luca, D. Fennema Galparsoro, G. Sancataldo, M. Leone, V. Foderà and V. Vetri, *J. Colloid Interface Sci.*, 2020, **574**, 229–240.

34 M. Ishigaki, K. Morimoto, E. Chatani and Y. Ozaki, *Biophys. J.*, 2020, **118**, 2997–3007.